

Article

Bi-Phase NiCo₂S₄-NiS₂/CFP Nanocomposites as a Highly Active Catalyst for Oxygen Evolution Reaction

Jintang Li , Yongji Xia, Xianrui Luo, Tianle Mao, Zhenjia Wang, Zheyu Hong and Guanghui Yue 

College of Materials, Xiamen University, Xiamen 361005, China

* Correspondence: leejt@xmu.edu.cn (J.L.); yuegh@xmu.edu.cn (G.Y.)

Abstract: Pursuing oxygen evolution reaction (OER) catalysts with high activity and stability is attracting many researchers. Here, we first designed and synthesized a biphasic three-dimensional structured catalyst of nickel–cobalt sulfide NiCo₂S₄-NiS₂/CFP, which is a nickel–cobalt sulfide composite decorated on carbon fiber paper (CFP) by a one-step hydrothermal method. It exhibited an overpotential of about 165 mV at a current density of 10 mA cm⁻² and a small Tafel slope of 81.54 mV dec⁻¹. Furthermore, the long-term stability of the NiCo₂S₄-NiS₂/CFP nanocomposite was 90.0% of the initial current density even after 12 h. The excellent catalytic performance of the NiCo₂S₄-NiS₂/CFP nanocomposite can be attributed to several aspects. Firstly, the petal-like morphology of the NiCo₂S₄-NiS₂ nanocomposite exposes more active sites. Secondly, the stability of the composite catalyst is significantly enhanced by its firm anchoring on the CFP. Thirdly, the catalytic performance was significantly improved by the addition of mixed valence of Ni or Co on the {111} plane of spinel NiCo₂S₄. Finally, the three-dimensional CFP substrate provides an efficient pathway and a stable integrated structure for the transmission of electrons and ions. Our one-step hydrothermal synthesis method provides a simple and economical way to obtain high-performance and robust OER catalysts.

Keywords: nickel–cobalt sulfide; oxygen evolution reaction; hydrothermal; electrocatalyst



Citation: Li, J.; Xia, Y.; Luo, X.; Mao, T.; Wang, Z.; Hong, Z.; Yue, G. Bi-Phase NiCo₂S₄-NiS₂/CFP Nanocomposites as a Highly Active Catalyst for Oxygen Evolution Reaction. *Coatings* **2023**, *13*, 313. <https://doi.org/10.3390/coatings13020313>

Academic Editors: Emerson Coy and Aivaras Kareiva

Received: 6 December 2022

Revised: 18 January 2023

Accepted: 20 January 2023

Published: 31 January 2023



Copyright: © 2023 by the authors. Licensee MDPI, Basel, Switzerland. This article is an open access article distributed under the terms and conditions of the Creative Commons Attribution (CC BY) license (<https://creativecommons.org/licenses/by/4.0/>).

1. Introduction

With today's society facing a severe fossil fuel energy crisis and environmental pollution, clean and sustainable energy sources are becoming a necessity for a highly civilized modern human society [1]. Therefore, searching for and developing new renewable energy sources is an urgent task at the moment [2–4]. The hydrogen energy which could be produced by water splitting [5,6] attracted the attention of many researchers because it is clean and inexpensive. However, owing to the kinetic sluggishness which results from four protons coupled with four-electron transfer in acidic and basic media, the efficiency of water splitting is greatly hindered by the half reaction oxygen evolution reaction (OER) [7–9]. RuO₂ and IrO₂ as the typical precious metal oxide catalysts are indicated as the state-of-the-art and best electrocatalysts for the OER, but the large-scale applications of those catalysts were blocked by their rareness and expensiveness [10,11]. Therefore, it is highly urgent and imperative to develop new and cheap electrocatalysts for OER with good electrochemical performance [12]. There are several ways to reduce the cost and improve the performance of catalysts, such as using metal doping [13], designing heterostructures [14] or deriving them from MOFs [15], which have been widely explored.

Recently, transition metal sulfides, which are abundant in the Earth's crust, have been widely investigated as potential OER catalysts due to their good electrical conductivity and high electrochemical activity [16–18]. However, some disadvantages of transition metal sulfides still limit their practical applications, such as scarce catalytic active sites, poor electron transport, low electrolyte contact efficiency and poor stability [19]. Many researchers have found that octahedral spinel structures contain more active sites than other structures, and thus are more likely to exhibit efficient catalytic activity [20–22]. It

is well known that NiCo_2S_4 , a typical material with octahedral spinel structure, always has good catalytic properties [23,24]. A number of researchers have reported single-phase NiCo_2S_4 [25–27], but bi-phase NiCo_2S_4 catalysts are rarely mentioned.

Herein, a bi-phase $\text{NiCo}_2\text{S}_4\text{-NiS}_2$ decorated on the surface of carbon fiber paper (CFP) was synthesized via a simple one-step hydrothermal method, and the as-synthesized nanocomposites were used as the catalysts for OER. Based on the high conductivity of electron/ion, larger specific surface areas, plentiful transfer channels of mass and excellent mechanical strength [28], CFP not only worked as an excellent conductive substrate but also provided a support 3D structure for catalyst anchoring [29]. The active material is grown directly on the CFP to form a self-supporting catalyst, which avoids the loss of active sites and the decrease in electron/ion transportation with additional binder of Nafion solution and additives [30,31]. A one-step hydrothermal synthesis method of catalysts is more efficient and cost effective [16,32]. As a conclusion, the electrocatalytic performance would be improved with the exposure of more active sites which could be realized on the $\text{NiCo}_2\text{S}_4\text{-NiS}_2/\text{CFP}$ catalyst. Here, the as-prepared $\text{NiCo}_2\text{S}_4\text{-NiS}_2/\text{CFP}$ catalyst indicated a lower overpotential of 165 mV with a current density of 10 mA cm^{-2} for OER, a small Tafel slope of $81.54 \text{ mV dec}^{-1}$ and a long-term stability of about 90.0% of its initial current density after 12 h.

2. Experimental Section

2.1. Reagents

All chemicals used in experiments were analytical reagents without further treatments. CFP was purchased from Dongli (Tianjin, China) Investment Co., Ltd. Cobalt nitrate hexahydrate ($\text{Co}(\text{NO}_3)_2 \cdot 6\text{H}_2\text{O}$), nickel acetate tetrahydrate ($\text{Ni}(\text{CH}_3\text{COO})_2 \cdot 4\text{H}_2\text{O}$), potassium hydroxide, nitric acid and thiourea were bought from Xilong Science Co., Ltd. (Chengdu, China) Anhydrous ethanol, IrO_2 powder and hydrochloric acid were bought from China Pharmaceutical Group Chemical Reagents Co., Ltd. (Shanghai, China) The dispersant sodium dodecyl sulfate (SDS) was supplied by Shantou Dahao Fine Chemicals Co., Ltd.

2.2. Treatment of CFP

First, a piece of CFP was cut into pieces with an area of $1.0 \times 1.0 \text{ cm}^2$. Second, the CFP sheets were immersed in aqua regia solution (8 mL 65% HNO_3 mixed with 24 mL 37% HCl) and kept in a fume hood at room temperature for 6 h [26] to get rid of metals which remained on the surface of the CFP, to form a functionalized and hydrophilic surface. Finally, processed CFP sheets were washed with distilled water thoroughly to obtain oxidized carbon fiber paper (OCFP).

2.3. Synthesis of $\text{NiCo}_2\text{S}_4\text{-NiS}_2/\text{CFP}$, $\text{Ni}_3\text{S}_4\text{-NiS}_2/\text{CFP}$ and $\text{Co}_2\text{S}/\text{CFP}$

All samples were synthesized by a hydrothermal method as follows and $\text{Ni}_3\text{S}_4\text{-NiS}_2/\text{CFP}$ and $\text{Co}_2\text{S}/\text{CFP}$ were also prepared in the same way as a reference group. Firstly, all solutions were prepared as shown for each solution listed in Table 1. Then, the solutions were transferred into a 100 mL Teflon-lined stainless-steel autoclave after being vigorously stirred for about half an hour, respectively. The autoclaves were kept at $220 \text{ }^\circ\text{C}$ for 12 h. After the autoclaves cooled to room temperature, the residues were collected with centrifugation and washed by anhydrous ethanol and deionized water three times, respectively. These three samples were dried in a vacuum desiccator at $80 \text{ }^\circ\text{C}$ for 12 h and denoted as $\text{NiCo}_2\text{S}_4\text{-NiS}_2/\text{CFP}$, $\text{Ni}_3\text{S}_4\text{-NiS}_2/\text{CFP}$ and $\text{Co}_2\text{S}/\text{CFP}$. The average mass loading of $\text{NiCo}_2\text{S}_4\text{-NiS}_2/\text{CFP}$, $\text{Ni}_3\text{S}_4\text{-NiS}_2/\text{CFP}$ and $\text{Co}_2\text{S}/\text{CFP}$ on substrates was 0.81 mg cm^{-2} , 0.75 mg cm^{-2} and 0.73 mg cm^{-2} , respectively.

Table 1. The synthesis of four kinds of sample.

Sample	Thiourea (mol)	Co ²⁺ (mmol)	Ni ²⁺ (mmol)	SDS (mmol)	DI Water (mL)
NiCo ₂ S ₄ -NiS ₂ /CFP	0.1	1.42	2.84	0.6	60
Ni ₃ S ₄ -NiS ₂ /CFP	0.1	/	4.26	0.6	60
Co ₂ S/CFP	0.1	4.26	/	0.6	60

2.4. Physical Characterization

The morphologies and compositions of samples were characterized by a field emission scanning electron microscope (FESEM, Hitachi SU-70, 10kV, Japan) equipped with an energy dispersive spectrometer (EDS, 20kV) analyzer. X-ray diffraction (XRD, Bruker, Germany) was implemented on a Bruker-AxsD8 X-ray diffractometer with a 2θ range from 10° to 90° . Rietveld refinement was accomplished by GSAS software. Transmission electron microscopy (TEM, Philips-FEI, Eindhoven, The Netherlands), high-resolution transmission electron microscopy (HRTEM), high-angle annular dark-field scanning transmission electron microscopy (HAADF-STEM) and corresponding energy dispersive spectroscopic (EDS) mapping analyses were all performed using a Talos F200s at 200 KV. X-ray photoelectron spectroscopy (XPS, USA) data were collected by using a PHI Quantum 2000 Scanning ESCA Microprobe with an Al X-ray source. The Raman measurement was performed in the XploRA microprobe Raman system (HORIBA, Kyoto, Japan).

2.5. Electrochemical Testing

All the electrochemical measurements were tested by employing an Autolab 302N in an electrochemistry workstation (Metrohm Autolab B.V., Utrecht, The Netherlands) at room temperature. The obtained CFP, NiCo₂S₄-NiS₂/CFP, Ni₃S₄-NiS₂/CFP and Co₂S/CFP were all cut into $0.5 \times 1 \text{ cm}^2$ pieces and employed as working electrodes directly. The IrO₂ working electrode was prepared with the follow steps. Firstly, 5 mg IrO₂ powder was dispersed into 1 mL solution (anhydrous ethanol/5 wt.% Nafion, 19:1, *v/v*). Then, the solution was ultrasonicated for more than 30 min to obtain a homogeneous solution. Finally, 20 μL of the homogeneous solution was dropped onto the surface of glassy carbon (diameter is 5 mm) to obtain the working electrode (the catalyst loading was $\sim 0.51 \text{ mg/cm}^2$). A mercuric oxide electrode and platinum (Pt) net were used as a reference electrode and counter electrode, respectively. The electrolyte was 1.0 M KOH (pH = 14). All measured potentials were calibrated with a reversible hydrogen electrode (RHE). The ultimate potential was calculated by the following equation: $E \text{ (vs. RHE)} = E \text{ (vs. Hg/HgO)} + 0.098 \text{ V} + 0.059 \text{ V} \cdot \text{pH}$. Linear sweep voltammetry (LSV) was manipulated at a scan rate 5 mV/s, ranging from 1.0 V to 2.0 V (vs. RHE). Cyclic voltammetry (CV) tests were carried out with a scan rate of 10 mV/s, 20 mV/s, 40 mV/s, 60 mV/s, 80 mV/s and 100 mV/s, respectively, in the range of 1.0–1.1 V (vs. RHE). The working electrodes were scanned several times for CV measurements at a scan rate 5 mV/s, ranging from 1.0 V to 2.0 V (vs. RHE) until the curves were steady for LSV and CV testing. Electrochemical impedance spectra (EIS) were conducted at open circuit voltage (OCP, shown on the screen of the system) vs. RHE with 5 mV AC amplitude and frequency ranging from 0.1 Hz to 100 kHz. The stability of as-prepared catalysts was assessed with a chronoamperometry test.

3. Results and Discussion

3.1. Synthesis and Characterization

During the hydrothermal reaction, oxidized OCFP was reduced to CFP again because of using the reducing reagent thiourea, thus NiCo₂S₄-NiS₂ particles were decorated and anchored on the surface of CFP after the hydrothermal reaction at 220 °C to form the NiCo₂S₄-NiS₂/CFP nanocomposites (Figure S1). The simple synthetic process is illustrated as a schematic diagram in Figure 1.

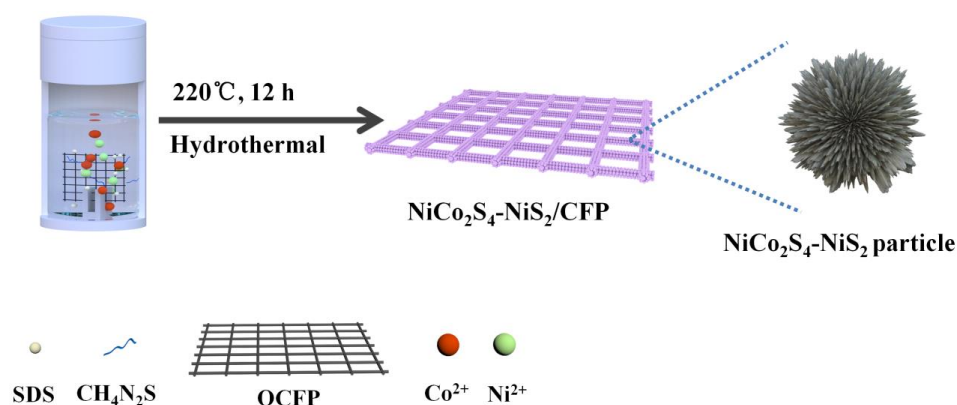


Figure 1. Schematic diagram showing the process for synthesizing NiCo₂S₄-NiS₂/CFP.

Figure 2 displays the morphology of the substrate and synthesized catalyst. Original commercial CFP was constituted by crossed microfibers with a diameter of approximately 7 μm and covered with carbon layers (Figure 2a), and a comparatively clear texture of the CFP can be found in Figure S2a,b. After being immersed in aqua regia for 6 h, CFP was oxidized into OCFP. It was detected that the surface of substrates had become smoother which means that metal impurities in CFP had been cleaned up without damaging the surface texture (Figure S2c,d). Petaloid-like NiCo₂S₄-NiS₂ with a diameter from 1 to 3 μm was formed by the aggregated NiCo₂S₄-NiS₂ nanowires, which were decorated and anchored on the surface of the CFP microfibers, as shown in Figure 2b,c. It can be found that the petaloid-like NiCo₂S₄-NiS₂ was distributed on the surface of the 3D skeleton of CFP uniformly, which makes the nanocomposites have a large specific surface and rough surface. The large specific surface, rough surface and the strong interaction may result in a good electrocatalytic performance of the as-synthesized NiCo₂S₄-NiS₂/CFP [33]. The morphologies of Ni₃S₄-NiS₂/CFP and CoS₂/CFP are shown in Figure S3a,b, respectively. The whole outline is the same as the sample of the NiCo₂S₄-NiS₂/CFP which is shown in Figure 2b. In Figure S3a,b, it can be seen that all Ni₃S₄-NiS₂ particles and CoS₂ particles are anchored on the surface of the CFP microfibers uniformly.

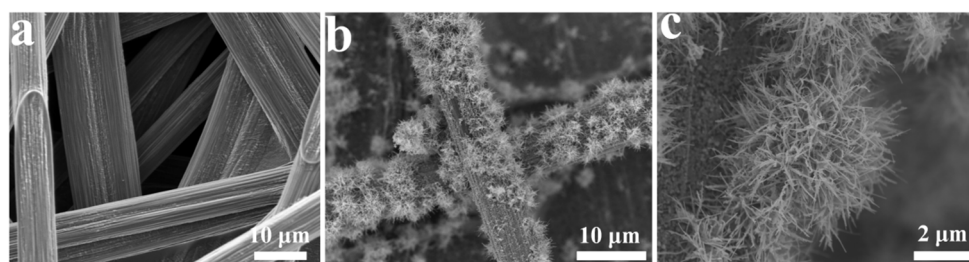


Figure 2. Morphologies of NiCo₂S₄-NiS₂/CFP. (a) SEM of CFP, (b,c) NiCo₂S₄-NiS₂/CFP.

The Rietveld refinement of XRD patterns of NiCo₂S₄-NiS₂ is shown in Figure 3. It suggests that the as-prepared electrocatalyst is composed of NiCo₂S₄ (JCPDS 20-0782) with a spinel structure (Fd-3m) and NiS₂ (JCPDS 73-0574). According to JCPDS 20-0782, the diffraction peak at 16.341° can be ascribed to the (111) plane of the NiCo₂S₄, which belongs to the {111} plane family of the spinel structure. Knözinger and Ratnasamy et al. [20,34] reported that the exposed octahedral cations in the {111} plane family of the spinel are more coordinated, resulting in better active catalytic performance. Furthermore, the weight percentages of NiCo₂S₄ phase and NiS₂ phase in the as-prepared catalyst are 87.34 wt% and 12.66 wt%, which were calculated by Rietveld structure refinement with GSAS software [35], as shown in Figure 3. The mole rate of NiCo₂S₄ phase and NiS₂ phase is 2.78:1, which means the spinel NiCo₂S₄ phase has a dominant position in the bi-phase NiCo₂S₄-NiS₂.

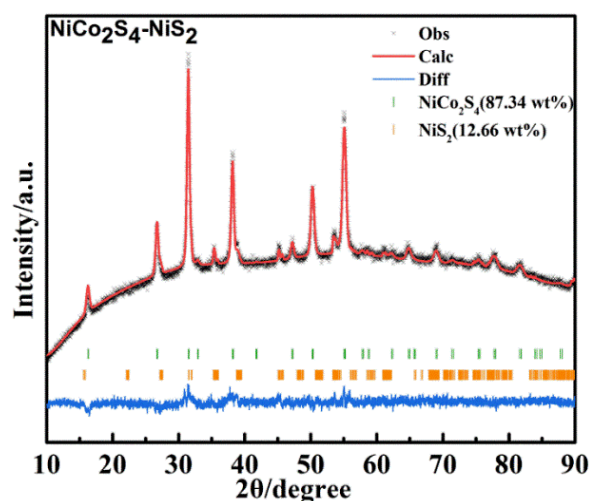


Figure 3. Rietveld refinement of XRD patterns of $\text{NiCo}_2\text{S}_4\text{-NiS}_2$.

The TEM image in Figure 4a shows that the petaloid-like $\text{NiCo}_2\text{S}_4\text{-NiS}_2$ is composed of many nanowires. The HRTEM image in the inset of Figure 4a shows that the petaloid-like $\text{NiCo}_2\text{S}_4\text{-NiS}_2$ nanocomposite is closely interlaced with NiCo_2S_4 and NiS_2 , and these small particles are interlaced and stacked to form distinct lattice dislocations. The planar spacing of NiCo_2S_4 is 0.542 nm, which corresponds to the (111) lattice plane. The adjacent planar spacing is 0.328 nm which is attributed to the NiS_2 (1-11) lattice plane. From the selected area electron diffraction (SAED) image of Figure 4b, the polycrystalline electron diffraction rings of $\text{NiCo}_2\text{S}_4\text{-NiS}_2$ could be traced to the planes of NiCo_2S_4 (JCPDS 20-0782) and NiS_2 (JCPDS 73-0574), which agree with the XRD pattern of $\text{NiCo}_2\text{S}_4\text{-NiS}_2$ in Figure 3. As can be seen in Figure 4c–f, the EDS patterns show the presence of uniform dispersion of Ni, Co and S in the petal-like $\text{NiCo}_2\text{S}_4\text{-NiS}_2$ nanocomposites. The XRD patterns of $\text{Ni}_3\text{S}_4\text{-NiS}_2$ and CoS_2 are displayed in Figure S4a,b, and it can be seen that the $\text{Ni}_3\text{S}_4\text{-NiS}_2$ is composed of Ni_3S_4 (JCPDS 76-1813) and NiS_2 (JCPDS 88-1709). The HRTEM, SAED and the corresponding EDX elemental mapping of $\text{Ni}_3\text{S}_4\text{-NiS}_2$ and CoS_2 are shown in Figures S5 and S6, respectively.

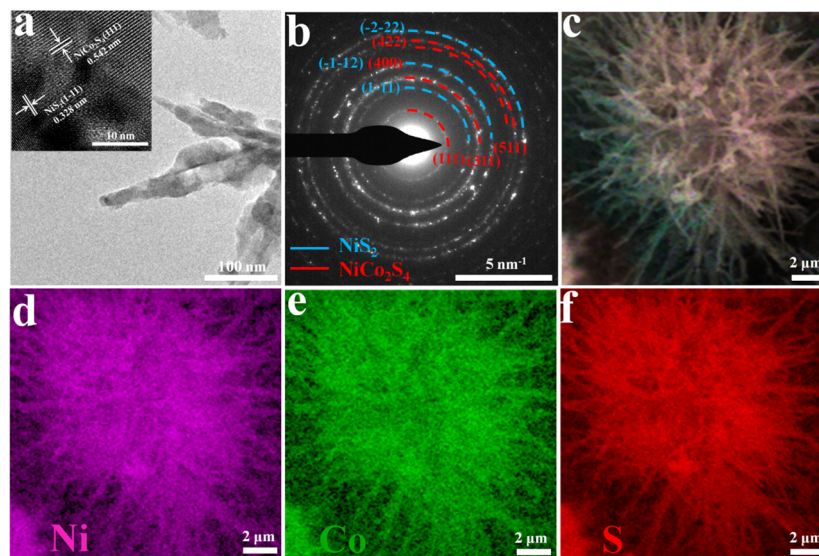


Figure 4. (a) The TEM image of $\text{NiCo}_2\text{S}_4\text{-NiS}_2$, the inset is HRTEM image of $\text{NiCo}_2\text{S}_4\text{-NiS}_2$. (b) Selected area electron diffraction (SAED) ring of $\text{NiCo}_2\text{S}_4\text{-NiS}_2$. (c–f) The area chosen for EDX elemental mapping of Ni, Co and S, respectively.

To further demonstrate that the NiCo₂S₄-NiS₂ particles were successfully immobilized on CFP, Raman spectroscopy was used to examine the NiCo₂S₄-NiS₂/CFP nanocomposites. The spectrum is shown in Figure S7, in which the strong peak which was located at around 1350 cm⁻¹ corresponds to the D band, which implies a disorder or defect site of the sp² carbon atoms. Meanwhile, the other peak at around 1590 cm⁻¹ can be attributed to the graphitic characteristic peak of the G band [36,37]. At the same time, the intensity of the D band/the intensity of the G band (I_D/I_G) indicates the degree of defects in carbon-based materials. I_D/I_G values of CFP, OCFP and NiCo₂S₄-NiS₂/CFP are 0.247, 0.105 and 0.657, respectively. To maintain energy stability, NiCo₂S₄-NiS₂ nanoparticles prefer to anchor and assemble on the defect sites of CFP, which further leads to the increase in defects in NiCo₂S₄-NiS₂/CFP nanocomposites. All these consequences proved that the NiCo₂S₄-NiS₂ nanocomposites had been successfully anchored on CFP and self-assembled as flower petals to expose many active sites. Moreover, the small peak detected at around 1620 cm⁻¹ (the red rectangle in Figure S7) in the CFP and NiCo₂S₄-NiS₂/CFP demonstrated OCFP was reduced to CFP during the hydrothermal reaction.

3.2. Electrocatalytic Testing

All the electrocatalytic performances of NiCo₂S₄-NiS₂/CFP nanocomposites were tested in 1M KOH solution. The NiCo₂S₄-NiS₂/CFP sample was used as a working electrode directly. The LSV curves are shown in Figure 5a, in which the NiCo₂S₄-NiS₂/CFP nanocomposites have the lowest overpotential of 165 mV at the current density of 10 mA cm⁻² in 1M KOH, compared to the Ni₃S₄-NiS₂/CFP nanocomposites (255 mV), the CoS₂/CFP nanocomposites (323 mV) and the commercial IrO₂ (368 mV). Electrocatalysis performance of NiCo₂S₄-NiS₂/CFP nanocomposites in this work is better than in other reported works which can be seen in Table S1. The OER activity of pure CFP was also tested for contrast, and a poor performance is revealed in Figure 5a. These results indicated that the high OER activity can be attributed to the transition metal sulfides. The large specific surface and rough surface provided by the petaloid spherules of NiCo₂S₄-NiS₂ nanocomposites have improved the electrocatalytic performance of the NiCo₂S₄-NiS₂/CFP. Compared with monometallic (Ni or Co) sulfide, the catalytic performance of the NiCo₂S₄-NiS₂/CFP nanocomposites could be improved by the synergistic effect of Ni and Co ions. Compared with Ni₃S₄-NiS₂/CFP, the catalytic performance of NiCo₂S₄-NiS₂/CFP could be boosted greatly with the existing spinel structure of NiCo₂S₄.

To study the catalytic kinetics of NiCo₂S₄-NiS₂/CFP, the Tafel slopes of all samples were determined from the LSV curves. According to the Tafel equation: $\eta = b \log j + c$, where η is the potential (V vs. RHE), j is the current density (mA cm⁻²), c is the constant, b is the Tafel slope. The Tafel slope b is an important parameter to understand the kinetic mechanism of OER, a smaller b means faster kinetics of OER. In Figure 5b, the NiCo₂S₄-NiS₂/CFP shows a Tafel slope of about 81.54 mV dec⁻¹, which is lower than for the CFP (211 mV dec⁻¹), Ni₃S₄-NiS₂/CFP (179 mV dec⁻¹) and CoS₂/CFP (218.35 mV dec⁻¹), with a value even lower than the noble-metal oxide IrO₂ (134.75 mV dec⁻¹). The ECSAs were estimated from C_{DL} measurements using CV scans at different scan rates (Figure S8). Results showed that NiCo₂S₄-NiS₂/CFP possessed the biggest double-layer capacitance of 4.66 mF cm⁻² which is consistent with the large surface area of the petaloid-like morphology in SEM images. The Nyquist plots of electrocatalysts were obtained for the OER half-cell at open circuit voltage vs. RHE with 5 mV AC amplitude and the results are shown in Figure 5c. The semi-circle represents the charge transfer resistance (R_{ct}) of electrocatalysts. It shows that R_{ct} of NiCo₂S₄-NiS₂/CFP is smaller than that of CFP, Ni₃S₄-NiS₂/CFP, CoS₂/CFP and IrO₂. The lower charge transfer resistance would prompt better electrocatalytic performance. The faster kinetic process of NiCo₂S₄-NiS₂/CFP can be attributed to the abundant proton transfer channels of CFP [28] and the mixed ions of Ni²⁺, Co²⁺ and Co³⁺ in the NiCo₂S₄-NiS₂/CFP nanocomposites (Figure 6a,b).

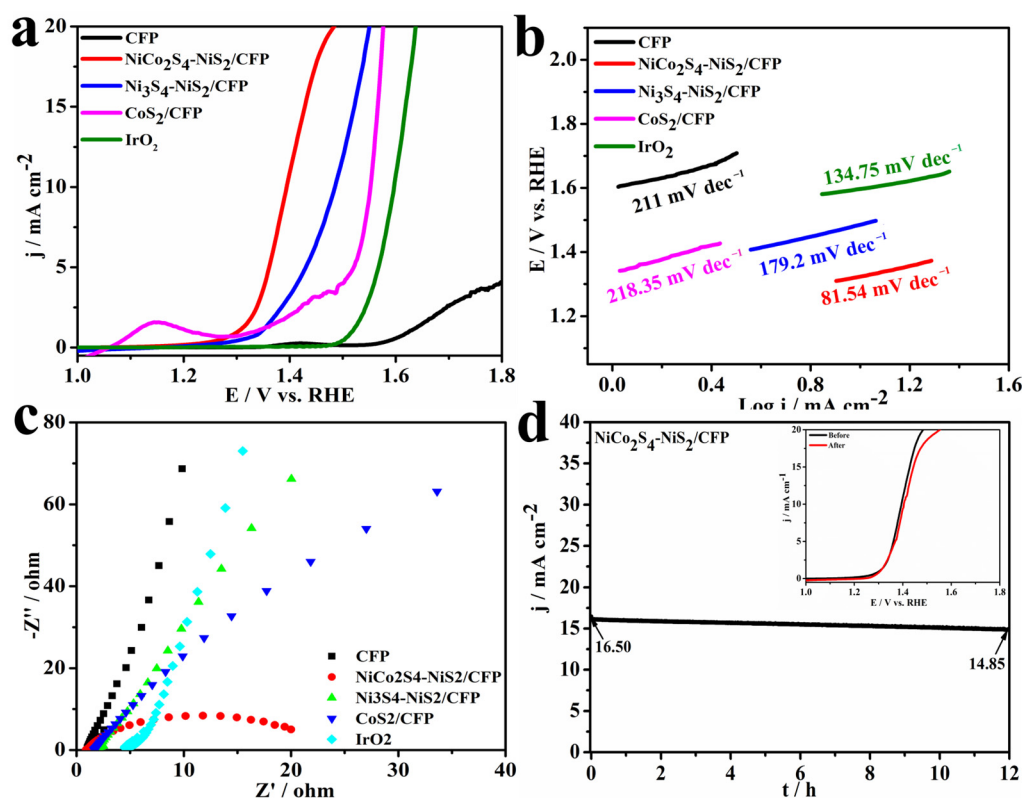


Figure 5. OER performance of NiCo₂S₄-NiS₂/CFP. (a) LSV of CFP, NiCo₂S₄-NiS₂/CFP, Ni₃S₄-NiS₂/CFP, CoS₂/CFP and commercial IrO₂. (b) Tafel slopes acquired from LSV in (a). (c) Nyquist plots of EIS. (d) The durability of NiCo₂S₄-NiS₂/CFP.

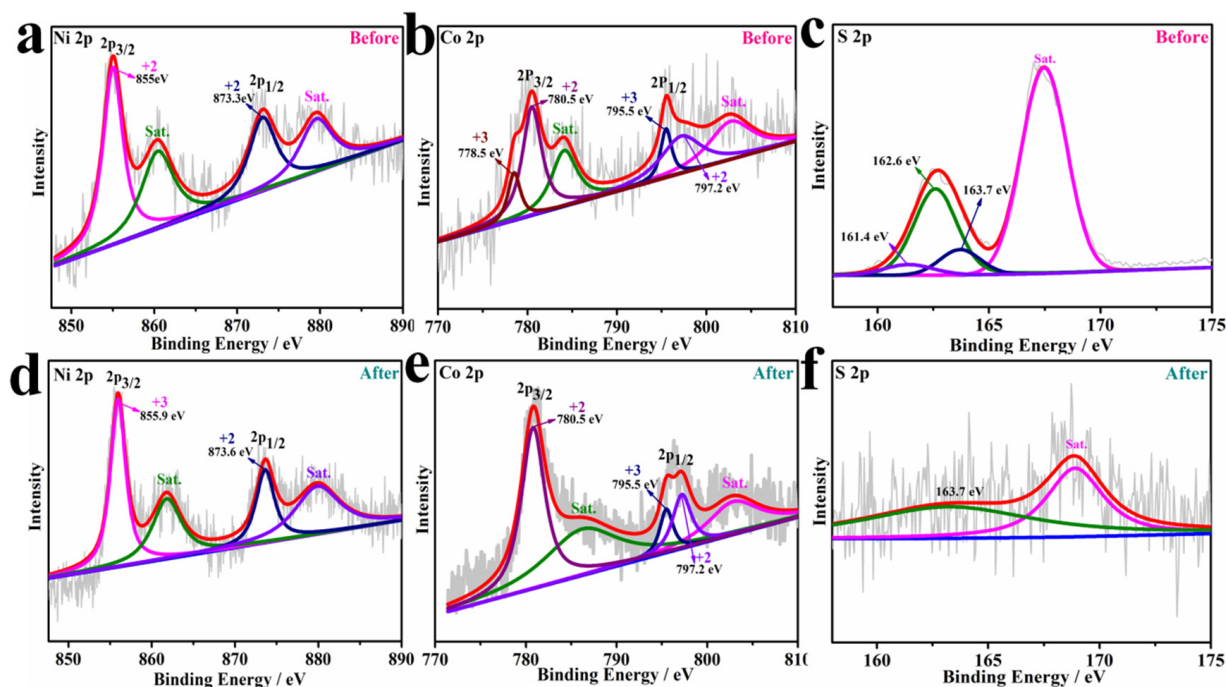


Figure 6. The XPS spectra of NiCo₂S₄-NiS₂/CFP before and after 12 h durability tests: (a,d) Ni 2p, (b,e) Co 2p and (c,f) S 2p.

Stability is an indispensable criterion for practical OER performance, so the long-term durability of the NiCo₂S₄-NiS₂/CFP sample was tested by chronoamperometric measurements at a constant potential of 1.4 V vs. RHE. As shown in Figure 5d, the

NiCo₂S₄-NiS₂/CFP nanocomposite retains an excellent durability of about 90.0% of the initial current density over a 12 h test. This can also be confirmed by the inset graphic in Figure 5d, showing the overpotential just increased a little bit after a 12 h durability test. Figure S9 reflects the morphology of NiCo₂S₄-NiS₂/CFP after a 12 h durability test, and the overall petaloid morphology is almost the same except the surface became smoother, resulting from NiCo₂S₄-NiS₂ nanocomposites strongly anchored on CFP to form a strong binding between NiCo₂S₄-NiS₂ and CFP.

To further confirm the composition changes in as-prepared NiCo₂S₄-NiS₂/CFP before and after a 12 h durability test, XPS measurement was employed. Figure 6a,d show the Ni 2p spectra of NiCo₂S₄-NiS₂/CFP before and after a 12 h durability test, and it can be seen that the outlines of two Ni 2p are almost the same. The peaks located at 855 eV, 873.3 eV and 873.6 eV all correspond to the Ni²⁺, the peaks located at 861.5 eV and 879.6 eV are labeled as the shake-up satellite peak [38,39] in Figure 6a,d. The peak located at 855.9 eV in Figure 6d is labeled as Ni³⁺, which means some Ni²⁺ was oxidized to Ni³⁺ after the 12 h durability test. The Co 2p spectra before and after the 12 h durability test are displayed in Figure 6b,e, in which the peaks at 778.5 eV and 795.5 eV are ascribed to Co³⁺ and the peaks at 780.5 eV and 797.2 eV are ascribed to Co²⁺ [24,40], meaning that Co ions appeared with mixed valence in the spinel structure NiCo₂S₄ of Ni₃S₄-NiS₂/CFP. Meanwhile, the peaks at 803 eV and 784.5 eV are ascribed to two satellite peaks [41]. Compared with Figure 6b, the peak located at 778.5 eV (see Figure 6e) disappeared, which means some Co³⁺ was reduced to Co²⁺ after the 12 h durability test. It is assumed that the excellent stability can be attributed to the spinel-structured Co³⁺ [17], and the 10% decrease in current density over the 12 h test could be ascribed to the reduction of Co³⁺ in NiCo₂S₄. A distinct change in S is observed in Figure 6c,f. Before the 12 h durability test, the peaks situated at 163.7 eV and 161.4 eV could be attributed to the characteristic peak of metal sulfide bonds and S²⁻ with low coordination, respectively [42,43]. The peak situated at 162.6 eV is attributed to bridging S₂²⁻ [44], which suggests that non-saturated S atoms existed in the Ni-S areas in the NiS₂ phase, and it is assumed that the presence of bridging S₂²⁻ may facilitate the protons' reduction and accelerate the electron transportation in the process of OER [17]. The peak situated at 167.4 eV is a satellite peak [45]. After the 12 h durability test, only a S²⁻ peak located at 163.7 eV and a satellite peak at 168.9 eV could be detected, as the peaks of S²⁻ and S₂²⁻ situated at 161.4 eV and 162.6 eV (see Figure 6c) disappeared. Those results revealed that S₂²⁻ and some S²⁻ were oxidized into hydroxide within the OER process [46]. This could be confirmed with the O XPS spectra and the EDS results of the catalyst before and after the 12 h durability test (see Figures S10 and S11). In Figure S10, the oxygen vacancy peaks disappear after the 12 h durability test, the peaks at 530.4 eV and 531.5 eV could be attributed to the hydroxyl-metal (Co-OH, Ni-OH) and the peak at 532.2 eV could be attributed to adsorbed oxygen [46,47]. The changes in the S and O atoms are revealed by Figure S11, in which the decrease in S and increase in O indicate that part of the S₂²⁻ and S²⁻ had been oxidized to form the hydroxyl, which also corroborates the XPS results.

Compared with Ni 2p spectrum of Ni₃S₄-NiS₂/CFP shown in Figure S12a and Co 2p spectrum of CoS₂/CFP shown in Figure S13a, the mixed valences of Ni²⁺, Co²⁺ and Co³⁺ existed in the catalyst NiCo₂S₄-NiS₂/CFP nanocomposites. The mixed metal valences can provide donor-acceptor chemisorption sites during the reversible adsorption of oxygen and then achieve relatively high electronic conductivity through valence electron hopping between cations [24,48].

The electrochemically effective surface area (ECSA) is also another parameter to evaluate the OER catalytic performance. It originated from double-layer capacitance (C_{dl}) on the catalyst surface, which satisfies the following equation: $ECSA = C_{dl}/C_s$ [49,50], while the value of C_s in 1 M KOH is 0.04 mF cm⁻². C_{dl} was calculated by cyclic voltammetry (CV) measured at scan rates from 10 to 100 mV/s. To obtain the currents related only to double-layer capacitance, scan rate-dependent CV was measured between 1.00 and 1.10 V (vs. RHE), where the redox processes do not occur (as shown in Figure 7). The $\Delta j = j_a - j_c$,

j_a and j_c were taken at 1.05 V vs. RHE. From the fitted linear slope, we calculated the C_{dl} which is half of the slope [51]. Figure 7a reflects that the fitted linear slope values ranked from high to low are $\text{NiCo}_2\text{S}_4\text{-NiS}_2/\text{CFP} > \text{IrO}_2 > \text{Ni}_3\text{S}_4\text{-NiS}_2/\text{CFP} > \text{CoS}_2/\text{CFP}$. This result suggested that the ECSA of the as-prepared catalyst $\text{NiCo}_2\text{S}_4\text{-NiS}_2/\text{CFP}$ is larger than that of the single metal (Ni and Co) sulfides and IrO_2 , and the catalyst with larger ECSA could produce more ion-accessible sites and exhibit better electrocatalytic activity.

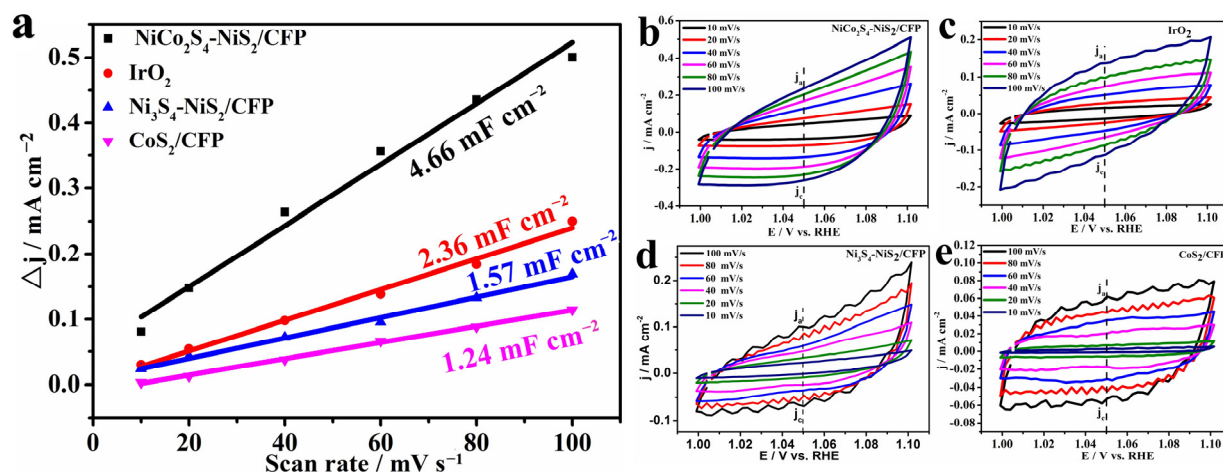


Figure 7. Electrochemical double-layer capacitances. (a) Linear fitting of Δj at 0.10 V vs. RHE as a function of the scan rate. (b) $\text{NiCo}_2\text{S}_4\text{-NiS}_2/\text{CFP}$. (c) IrO_2 . (d) $\text{Ni}_3\text{S}_4\text{-NiS}_2/\text{CFP}$. (e) CoS_2/CFP .

4. Conclusions

Here, petaloid-structured bi-phase bimetal sulfide catalyst $\text{NiCo}_2\text{S}_4\text{-NiS}_2/\text{CFP}$ nanocomposites were synthesized by a simple hydrothermal method successfully. Compared with the monometallic (Ni or Co) sulfide with CFP, $\text{NiCo}_2\text{S}_4\text{-NiS}_2/\text{CFP}$ exhibits remarkable performance with a low overpotential of 165 mV at a current density of 10 mA cm^{-2} in alkaline solution, and also a detectable Tafel slope of $81.54 \text{ mV dec}^{-1}$. Under similar conditions, the overpotential of the synthesized $\text{NiCo}_2\text{S}_4\text{-NiS}_2/\text{CFP}$ is lower than that of most recently reported electrocatalysts for OER. Meanwhile, a retention rate of 90.0% could be obtained when the catalyst was tested for 12 h. The superior performance of the as-prepared $\text{NiCo}_2\text{S}_4\text{-NiS}_2/\text{CFP}$ nanocomposites benefits from several factors, including the special petaloid morphology and 3D structure provided by the CFP substrate, the strong coupling effect between spinel NiCo_2S_4 and NiS_2 , the mixed valence of Ni and Co and the exposed active sites on the {111} plane. Furthermore, this work offers a simple and economical way via a hydrothermal method to obtain efficient and robust spinel NiCo_2S_4 base catalysts for OER.

Supplementary Materials: The following supporting information can be downloaded at: <https://www.mdpi.com/article/10.3390/coatings13020313/s1>, Figure S1. The surface change after as prepared $\text{NiCo}_2\text{S}_4\text{-NiS}_2$ anchored on the surface of CFP; Figure S2. Low-magnification SEM images of (a) CFP and (c) OCFP. High-magnification SEM images of (b) CFP and (d) OCFP; Figure S3. The morphologies of (a) $\text{Ni}_3\text{S}_4\text{-NiS}_2/\text{CFP}$ and (b) CoS_2/CFP ; Figure S4. XRD patterns of (a) $\text{Ni}_3\text{S}_4\text{-NiS}_2$ and (b) CoS_2 ; Figure S5. (a,b) HRTEM image of $\text{Ni}_3\text{S}_4\text{-NiS}_2$. (c,d) Selected area electron diffraction (SAED) diffraction ring of $\text{Ni}_3\text{S}_4\text{-NiS}_2$. (e,f) The area chosen to do EDX elemental mapping and the corresponding EDX elemental mapping images for Ni and S respectively; Figure S6. (a) The TEM image of CoS_2 . (b) HRTEM image of CoS_2 . (c,d) Selected area electron diffraction (SAED) diffraction ring of CoS_2 . (e,f) The area chosen to do EDX elemental mapping and the corresponding EDX elemental mapping images for Co and S respectively; Figure S7. Raman spectra of CFP, OCFP and $\text{NiCo}_2\text{S}_4\text{-NiS}_2/\text{CFP}$; Figure S8. Double-layer capacitances (a) and CV scans at different scan rates (b–e); Figure S9. The morphology of $\text{NiCo}_2\text{S}_4\text{-NiS}_2/\text{CFP}$ after 12 h durability test; Figure S10. The O XPS spectra of as-prepared catalyst before (a) and after (b) 12 h durability test; Figure S11. The EDS results of $\text{NiCo}_2\text{S}_4\text{-NiS}_2/\text{CFP}$ (a) before 12 h durability test. (b) After 12 h durability test; Figure S12.

The XPS spectra of (a) Ni 2p, (b) S 2p in Ni₃S₄-NiS₂/CFP; Figure S13. The XPS spectra of (a) Co 2p, (b) S 2p in CoS₂/CFP; Table S1. Comparison of OER activity of NiCo₂S₄-NiS₂/CFP with that of most reported nick-el-cobalt sulfide catalysts tested in alkaline solution [52–58].

Author Contributions: Conceptualization, writing—review and editing, J.L.; methodology, Y.X., X.L., and T.M.; formal analysis, Y.X., Z.W. and Z.H.; supervision and funding acquisition, G.Y. All authors have read and agreed to the published version of the manuscript.

Funding: This research was funded by the National Natural Science Foundation of China (Grant No. 51971184), the Natural Science Foundation of Fujian Province of China (No. 2021J01043).

Institutional Review Board Statement: Not applicable.

Informed Consent Statement: Not applicable.

Data Availability Statement: Not applicable.

Conflicts of Interest: The authors declare have no conflict of interest.

References

1. Yang, T.L.; Xia, Y.J.; Mao, T.L.; Ding, Q.W.; Wang, Z.J.; Hong, Z.Y.; Han, J.J.; Peng, D.L.; Yue, G.H. Phosphorus Vacancies and Heterojunction Interface as Effective Lithium-Peroxide Promoter for Long-Cycle Life Lithium–Oxygen Batteries. *Adv. Funct. Mater.* **2022**, *32*, 2209876. [[CrossRef](#)]
2. Dutta, S.; Indra, A.; Feng, Y.; Han, H.; Song, T. Promoting electrocatalytic overall water splitting with nanohybrid of transition metal nitride-oxynitride. *Appl. Catal. B Environ.* **2019**, *241*, 521–527. [[CrossRef](#)]
3. Hu, C.; Dai, L. Multifunctional Carbon-Based Metal-Free Electrocatalysts for Simultaneous Oxygen Reduction, Oxygen Evolution, and Hydrogen Evolution. *Adv. Mater.* **2017**, *29*, 1604942. [[CrossRef](#)]
4. Sathiskumar, C.; Ramakrishnan, S.; Vinothkannan, M.; Karthikeyan, S.; Yoo, D.J.; Kim, A.R. Nitrogen-Doped Porous Carbon Derived from Biomass Used as Trifunctional Electrocatalyst toward Oxygen Reduction, Oxygen Evolution and Hydrogen Evolution Reactions. *Nanomaterials* **2019**, *10*, 76. [[CrossRef](#)] [[PubMed](#)]
5. Hu, C.G.; Chen, X.Y.; Dai, Q.B.; Wang, M.; Qu, L.T.; Dai, L.M. Earth-Abundant Carbon Catalysts for Renewable Generation of Clean Energy from Sunlight and Water. *Nano Energy* **2017**, *41*, 367–376. [[CrossRef](#)]
6. Xia, G.; Li, D.; Chen, X.; Tan, Y.; Tang, Z.; Guo, Z.; Liu, H.; Liu, Z.; Yu, X. Carbon-Coated Li₃N Nanofibers for Advanced Hydrogen Storage. *Adv. Mater.* **2013**, *25*, 6238–6244. [[CrossRef](#)] [[PubMed](#)]
7. Koper, M.T.M. Thermodynamic theory of multi-electron transfer reactions: Implications for electrocatalysis. *J. Electroanal. Chem.* **2011**, *660*, 254–260. [[CrossRef](#)]
8. Jiao, Y.; Zheng, Y.; Jaroniec, M.; Qiao, S.Z. Design of Electrocatalysts for Oxygen- and Hydrogen-Involving Energy Conversion Reactions. *Chem. Soc. Rev.* **2015**, *44*, 2060–2086. [[CrossRef](#)]
9. Zhao, H.H.; Yang, Y.; Dai, X.P.; Qiao, H.Y.; Yong, J.X.; Luan, X.B.; Yu, L.; Luan, C.L.; Wang, Y.; Zhang, X. Nico-Dh Nanodots Anchored on Amorphous Nico-Sulfide Sheets as Efficient Electrocatalysts for Oxygen Evolution Reaction. *Electrochim. Acta* **2019**, *295*, 1085–1092. [[CrossRef](#)]
10. Zhu, Y.P.; Liu, Y.P.; Ren, T.Z.; Yuan, Z.Y. Self-Supported Cobalt Phosphide Mesoporous Nanorod Arrays: A Flexible and Bifunctional Electrode for Highly Active Electrocatalytic Water Reduction and Oxidation. *Adv. Funct. Mater.* **2015**, *25*, 7337–7347. [[CrossRef](#)]
11. Xu, W.; Lu, Z.; Lei, X.; Li, Y.; Sun, X. A Hierarchical Ni-Co-O@Ni-Co-S Nanoarray as an Advanced Oxygen Evolution Reaction Electrode. *Phys. Chem. Chem. Phys.* **2014**, *16*, 20402–20405. [[CrossRef](#)] [[PubMed](#)]
12. Wang, C.; Zhao, Y.; Liu, J.; Gong, P.; Li, X.; Zhao, Y.; Yue, G.; Zhou, Z. Highly Hierarchical Porous Structures Constructed from NiO Nanosheets Act as Li Ion and O(2) Pathways in Long Cycle Life, Rechargeable Li-O(2) Batteries. *Chem. Commun.* **2016**, *52*, 11772–11774. [[CrossRef](#)]
13. Alburaih, H.A.; Ansari, M.Z.; Abid, A.G.; Khosa, R.Y.; Ashiq, M.N.; Manzoor, S.; Aman, S.; Chaudhry, H.; Waheed, M.S.; Taha, T.A. Study on active sites of Mn-doped iron selenide on pencil electrode for electrocatalytic water splitting. *J. Sol-Gel Sci. Technol.* **2022**, *11*, 1–9. [[CrossRef](#)]
14. Khan, M.T.N.; Ahmed, F.; Houda, S.; Manzoor, S.; Hasnain, K.; Zahra, M.; Hussain, R.; Ansari, M.Z.; Hegazy, H.H.; Ashiq, M.N. Facile synthesis of novel Ag@cerium zirconate heterostructure for efficient oxygen evolution reaction. *Surf. Interfaces* **2022**, *35*, 102410–102420. [[CrossRef](#)]
15. Owidah, Z.O.; Aman, S.; Abdullah, M.; Manzoor, S.; Fallatah, A.M.; Ibrahim, M.M.; Elnasr, T.A.S.; Ansari, M.Z. Metal oxide/carbon nanosheet arrays derivative of stacked metal organic frameworks for triggering oxygen evolution reaction. *Ceram. Int.* **2022**, *49*, 5936–5943. [[CrossRef](#)]
16. Chen, H.; Jiang, J.; Zhang, L.; Wan, H.; Qi, T.; Xia, D. Highly conductive NiCo₂S₄ urchin-like nanostructures for high-rate pseudocapacitors. *Nanoscale* **2013**, *5*, 8879–8883. [[CrossRef](#)]

17. Jing, F.; Lv, Q.Y.; Xiao, J.; Wang, Q.J.; Wang, S. Highly Active and Dual-Function Self-Supported Multiphase Ni-Ni₂-Ni₃S₂/Ni Electrodes for Overall Water Splitting. *J. Mater. Chem. A* **2018**, *6*, 14207–14214. [[CrossRef](#)]
18. Chinnadurai, D.; Manivelan, N.; Prabakar, K. Modulating the Intrinsic Electrocatalytic Activity of Copper Sulfide by Silver Doping for Electrocatalytic Overall Water Splitting. *Chemelectrochem* **2022**, *9*, e202200254. [[CrossRef](#)]
19. Viswanathan, V.; Pickrahn, K.L.; Luntz, A.C.; Bent, S.F.; Norskov, J.K. Nanoscale Limitations in Metal Oxide Electrocatalysts for Oxygen Evolution. *Nano Lett.* **2014**, *14*, 5853–5857. [[CrossRef](#)] [[PubMed](#)]
20. Chauhan, M.; Reddy, K.P.; Gopinath, C.S.; Deka, S. Copper Cobalt Sulfide Nanosheets Realizing a Promising Electrocatalytic Oxygen Evolution Reaction. *ACS Catal.* **2017**, *7*, 5871–5879. [[CrossRef](#)]
21. Jacobs, J.P.; Maltha, A.; Reintjes, J.G.H.; Drimal, J.; Ponec, V.; Brongersma, H.H. The Surface of Catalytically Active Spinels. *J. Catal.* **1994**, *147*, 294–300. [[CrossRef](#)]
22. Liu, Y.; Xiao, C.; Lyu, M.; Lin, Y.; Cai, W.; Huang, P.; Tong, W.; Zou, Y.; Xie, Y. Ultrathin Co₃S₄ Nanosheets that Synergistically Engineer Spin States and Exposed Polyhedra that Promote Water Oxidation under Neutral Conditions. *Angew. Chem. Int. Ed.* **2015**, *54*, 11231–11235. [[CrossRef](#)] [[PubMed](#)]
23. Liu, D.; Lu, Q.; Luo, Y.; Sun, X.; Asiri, A.M. NiCo₂S₄ nanowires array as an efficient bifunctional electrocatalyst for full water splitting with superior activity. *Nanoscale* **2015**, *7*, 15122–15126. [[CrossRef](#)]
24. Liu, Q.; Jin, J.; Zhang, J. NiCo₂S₄@Graphene as a Bifunctional Electrocatalyst for Oxygen Reduction and Evolution Reactions. *ACS Appl. Mater. Interfaces* **2013**, *5*, 5002–5008. [[CrossRef](#)]
25. Li, F.; Xu, R.C.; Li, Y.M.; Liang, F.; Zhang, D.F.; Fu, W.F.; Lv, X.J. N-doped carbon coated NiCo₂S₄ hollow nanotube as bifunctional electrocatalyst for overall water splitting. *Carbon* **2019**, *145*, 521–528. [[CrossRef](#)]
26. Feng, X.; Jiao, Q.; Cui, H.; Yin, M.; Li, Q.; Zhao, Y.; Li, H.; Zhou, W.; Feng, C. One-Pot Synthesis of NiCo₂S₄ Hollow Spheres via Sequential Ion-Exchange as an Enhanced Oxygen Bifunctional Electrocatalyst in Alkaline Solution. *ACS Appl. Mater. Interfaces* **2018**, *10*, 29521–29531. [[CrossRef](#)] [[PubMed](#)]
27. Kang, Z.; Guo, H.J.; Wu, J.; Sun, X.; Zhang, Z.; Liao, Q.L.; Zhang, S.C.; Si, H.N.; Wu, P.W.; Wang, L.; et al. Engineering an Earth-Abundant Element-Based Bifunctional Electrocatalyst for Highly Efficient and Durable Overall Water Splitting. *Adv. Funct. Mater.* **2019**, *29*, 1807031. [[CrossRef](#)]
28. Khan, Z.; Senthilkumar, B.; O Park, S.; Park, S.; Yang, J.; Lee, J.H.; Song, H.K.; Kim, Y.; Kwak, S.K.; Ko, H. Carambola-shaped VO₂ nanostructures: A binder-free air electrode for an aqueous Na-air battery. *J. Mater. Chem. A* **2017**, *5*, 2037–2044. [[CrossRef](#)]
29. Ma, T.T.; Dai, Z.; Shen, X.R.; Jiao, Q.Z.; Zhao, Y.; Li, H.S.; Feng, C.H. Three-Dimensional Porous MnCo₂S₄ Microrugby Balls Supported on Carbon Cloth for Efficient Oxygen Evolution Reaction. *Chemelectrochem* **2022**, *9*, e202200552. [[CrossRef](#)]
30. Zhong, M.X.; Song, N.; Li, C.M.; Wang, C.; Chen, W.; Lu, X.F. Controllable Growth of Fe-Doped Ni₂ on NiFe-Carbon Nanofibers for Boosting Oxygen Evolution Reaction. *J. Colloid Interface Sci.* **2022**, *614*, 556–565. [[CrossRef](#)]
31. Zhou, X.C.; Yang, H.; Rao, D.W.; Yan, X.H. Morphology Controllable NiCo₂S₄ Nanostructure on Carbon Cloth for Enhanced Electrocatalytic Water Oxidation. *J. Alloys Compd.* **2022**, *897*, 163152. [[CrossRef](#)]
32. Nguyen, V.H.; Shim, J.-J. In situ growth of hierarchical mesoporous NiCo₂S₄@MnO₂ arrays on nickel foam for high-performance supercapacitors. *Electrochim. Acta* **2015**, *166*, 302–309. [[CrossRef](#)]
33. Zhang, X.Q.; Zhao, Y.C.; Wang, C.G.; Li, X.; Liu, J.D.; Yue, G.H.; Zhou, Z.D. Facile synthesis of hollow urchin-like NiCo₂O₄ microspheres for high-performance sodium-ion batteries. *J. Mater. Sci.* **2016**, *51*, 9296–9305. [[CrossRef](#)]
34. Knözinger, H.; Ratnasamy, P. Catalytic Aluminas: Surface Models and Characterization of Surface Sites. *Catal. Rev.* **1978**, *17*, 31–70. [[CrossRef](#)]
35. Toby, B.H. Expgui, a Graphical User Interface for Gsas. *J. Appl. Crystallogr.* **2001**, *34*, 210–213. [[CrossRef](#)]
36. Li, Z.Q.; Lu, C.J.; Xia, Z.P.; Zhou, Y.; Luo, Z. X-ray diffraction patterns of graphite and turbostratic carbon. *Carbon* **2007**, *45*, 1686–1695. [[CrossRef](#)]
37. Pimenta, M.A.; Dresselhaus, G.; Dresselhaus, M.S.; Cañado, L.G.; Jorio, A.; Saito, R. Studying disorder in graphite-based systems by Raman spectroscopy. *Phys. Chem. Chem. Phys.* **2007**, *9*, 1276–1290. [[CrossRef](#)]
38. Su, Y.Z.; Xiao, K.; Li, N.; Liu, Z.Q.; Qiao, S.Z. Amorphous Ni(OH)₂ @ three-dimensional Ni core-shell nanostructures for high capacitance pseudocapacitors and asymmetric supercapacitors. *J. Mater. Chem. A* **2014**, *2*, 13845–13853. [[CrossRef](#)]
39. Wu, Z.C.; Wang, X.; Huang, J.S.; Gao, F. A Co-doped Ni-Fe mixed oxide mesoporous nanosheet array with low overpotential and high stability towards overall water splitting. *J. Mater. Chem. A* **2018**, *6*, 167–178. [[CrossRef](#)]
40. Shuai, C.; Mo, Z.L.; Niu, X.H.; Yang, X.; Liu, G.G.; Wang, J.; Liu, N.J.; Guo, R.B. Hierarchical NiCo₂S₄ nanosheets grown on graphene to catalyze the oxygen evolution reaction. *J. Mater. Sci.* **2020**, *55*, 1627–1636. [[CrossRef](#)]
41. Wu, X.Y.; Li, S.M.; Wang, B.; Liu, J.H.; Yu, M. Graphene Foam Supported Multilevel Network-Like NiCo₂S₄ Nanoarchitectures for Robust Lithium Storage and Efficient Orr Catalysis. *New J. Chem.* **2017**, *41*, 115–125. [[CrossRef](#)]
42. Yin, J.L.; Zhang, H.; Luo, J.Q.; Yao, M.Q.; Hu, W.C. High-boiling-point solvent synthesis of mesoporous NiCo₂S₄ with high specific surface area as supercapacitor electrode material. *J. Mater. Sci. Mater. Electron.* **2017**, *28*, 2093–2099. [[CrossRef](#)]
43. Du, W.M.; Wang, Z.Y.; Zhu, Z.Q.; Hu, S.; Zhu, X.Y.; Shi, Y.F.; Pang, H.; Qian, X.F. Facile Synthesis and Superior Electrochemical Performances of NiCo₂S₄/Graphene Nanocomposite Suitable for Supercapacitor Electrodes. *J. Mater. Chem. A* **2014**, *2*, 9613–9619. [[CrossRef](#)]

44. Liu, N.; Guo, Y.; Yang, X.; Lin, H.; Yang, L.; Shi, Z.; Zhong, Z.; Wang, S.; Tang, Y.; Gao, Q. Microwave-Assisted Reactant-Protecting Strategy toward Efficient MoS₂ Electrocatalysts in Hydrogen Evolution Reaction. *ACS Appl. Mater. Interfaces* **2015**, *7*, 23741–23749. [[CrossRef](#)]
45. Jiang, J.Y.; Yan, C.Y.; Zhao, X.H.; Luo, H.X.; Xue, Z.M.; Mu, T.C. A PEGylated deep eutectic solvent for controllable solvothermal synthesis of porous NiCo₂S₄ for efficient oxygen evolution reaction. *Green Chem.* **2017**, *19*, 3023–3031. [[CrossRef](#)]
46. Yuan, F.F.; Wei, J.D.; Qin, G.X.; Ni, Y.H. Carbon Cloth Supported Hierarchical Core-Shell NiCo₂S₄@Coni-Ldh Nanoarrays as Catalysts for Efficient Oxygen Evolution Reaction in Alkaline Solution. *J. Alloys Compd.* **2020**, *830*, 154658. [[CrossRef](#)]
47. Liu, Y.; Bai, Y.; Han, Y.; Yu, Z.; Zhang, S.; Wang, G.; Wei, J.; Wu, Q.; Sun, K. Self-Supported Hierarchical Fecon-Lth/NiCo₂O₄/Cc Electrodes with Enhanced Bifunctional Performance for Efficient Overall Water Splitting. *ACS Appl. Mater. Interfaces* **2017**, *9*, 36917–36926. [[CrossRef](#)]
48. Hamdani, M.; Singh, R.N.; Chartier, P. Co₃O₄ and Co- Based Spinel Oxides Bifunctional Oxygen Electrodes. *Int. J. Electrochem. Sci.* **2010**, *5*, 556–577.
49. McCrory, C.C.; Jung, S.; Peters, J.C.; Jaramillo, T.F. Benchmarking Heterogeneous Electrocatalysts for the Oxygen Evolution Reaction. *J. Am. Chem. Soc.* **2013**, *135*, 16977–16987. [[CrossRef](#)]
50. Trasatti, S.; Petrii, O.A. Real Surface Area Measurements in Electrochemistry. *J. Electroanal. Chem.* **1992**, *327*, 353–376. [[CrossRef](#)]
51. Zhan, T.R.; Liu, X.L.; Lu, S.S.; Hou, W.G. Nitrogen doped NiFe layered double hydroxide/reduced graphene oxide mesoporous nanosphere as an effective bifunctional electrocatalyst for oxygen reduction and evolution reactions. *Appl. Catal. B Environ.* **2017**, *205*, 551–558. [[CrossRef](#)]
52. Darband, G.B.; Aliofkhaezrai, M.; Hyun, S.; Rouhaghdam, A.S.; Shanmugam, S. Electrodeposition of Ni-Co-Fe mixed sulfide ultrathin nanosheets on Ni nanocones: A low-cost, durable and high performance catalyst for electrochemical water splitting. *Nanoscale* **2019**, *11*, 16621–16634. [[CrossRef](#)] [[PubMed](#)]
53. Hong, Y.R.; Mhin, S.; Kim, K.M.; Han, W.S.; Choi, H.; Ali, G.; Chung, K.Y.; Lee, H.J.; Moon, S.I.; Dutta, S.; et al. Electrochemically activated cobalt nickel sulfide for an efficient oxygen evolution reaction: Partial amorphization and phase control. *J. Mater. Chem. A* **2019**, *7*, 3592–3602. [[CrossRef](#)]
54. Zou, H.; He, B.; Kuang, P.; Yu, J.; Fan, K. Metal-Organic Framework-Derived Nickel-Cobalt Sulfide on Ultrathin Mxene Nanosheets for Electrocatalytic Oxygen Evolution. *ACS Appl. Mater. Interfaces* **2018**, *10*, 22311–22319. [[CrossRef](#)] [[PubMed](#)]
55. Tang, Y.; Yang, H.; Sun, J.; Xia, M.; Guo, W.; Yu, L.; Yan, J.; Zheng, J.; Chang, L.; Gao, F. Phase-pure Pentlandite Ni_{4.3}Co_{4.7}S₈ Binary Sulfide as Efficient Bifunctional Electrocatalyst for Oxygen Evolution and Hydrogen Evolution. *Nanoscale* **2018**, *10*, 10459–10466. [[CrossRef](#)] [[PubMed](#)]
56. Qin, K.; Wang, L.; Wen, S.; Diao, L.; Liu, P.; Li, J.; Ma, L.; Shi, C.; Zhong, C.; Hu, W.; et al. Designed synthesis of NiCo-LDH and derived sulfide on heteroatom-doped edge-enriched 3D rivet graphene films for high-performance asymmetric supercapacitor and efficient OER. *J. Mater. Chem. A* **2018**, *6*, 8109–8119. [[CrossRef](#)]
57. Zhao, C.; Li, P.; Shao, D.; Zhang, R.; Wang, S.; Zhu, Z.; Zhao, C. Phytic acid-derived Co_{2-x}Ni_xP₂O₇-C/RGO and its superior OER electrocatalytic performance. *Int. J. Hydrog. Energy* **2019**, *44*, 844–852. [[CrossRef](#)]
58. Yu, Z.; Bai, Y.; Zhang, S.; Liu, Y.; Zhang, N.; Sun, K. MOF-directed templating synthesis of hollow nickel-cobalt sulfide with enhanced electrocatalytic activity for oxygen evolution. *Int. J. Hydrog. Energy* **2018**, *43*, 8815–8823. [[CrossRef](#)]

Disclaimer/Publisher's Note: The statements, opinions and data contained in all publications are solely those of the individual author(s) and contributor(s) and not of MDPI and/or the editor(s). MDPI and/or the editor(s) disclaim responsibility for any injury to people or property resulting from any ideas, methods, instructions or products referred to in the content.